Position Reconstruction and Charge Distribution in LHCb VELO Silicon Sensors

T.W. Versloot[a], A. Papadelis[a,1], K. Akiba[b,c], M. Artuso[d], M. van Beuzekom[a], J. Borel[e], T.J.V. Bowcock[f], J. Buytaert[d], P. Collins[b], R. Dumps[b], L. Dwyer[f], D. Eckstein[b], L. Eklund[g], M. Ferro-Luzzi[b], R. Frei[e], M. Gersabeck[g], G. Haefeli[e], K. Hennessy[h], T. Huse[f], E. Jans[a], M. John[b], T.J. Ketel[i], A. Keune[a], T. Laštovička[b], R. Mountain[d], N. Neufeld[b], C. Parkes[g], S. Stone[d], T. Szumlak[g], M. Tobin[f], A. Van Lysebetten[a], S. Viret[g], H. de Vries[a], J. Wang[d].

[a] NIKHEF, Amsterdam
[b] CERN
[c] Universidade Federal do Rio de Janeiro
[d] Syracuse University
[e] École Polytechnique Fédérale de Lausanne
[f] University of Liverpool
[g] University of Glasgow
[h] University College Dublin
[i] Vrije Universiteit Amsterdam

Abstract

In 2006, a partially equipped LHCb VELO detector half was characterised in a test beam experiment (Alignment Challenge and Detector Commissioning, ACDC3). The position reconstruction and resolution for 2-strip R-sensor clusters was studied as a function of strip pitch (p) and track inclination (θ) on the sensor surface. The Charge Density Distribution (CDD) is derived from the weighted charge distribution. It becomes asymmetric for tracks non-perpendicular to the strip surface.

It is shown that the asymmetric broadening of the CDD around the track intercept position results in a linear η-function at higher angles ($> 6^o$). The sensor spatial resolution (σ_s) is determined both using a linear weighted mean of strip charges, as well as a third-order polynomial approximation via a $\eta(x)$-correction. The best R-sensor resolutions obtained are:

Method	Strip pitch, p	Angle, θ	Spatial resolution, σ_s
Weighted mean	(45 ± 5) μm	$(0-1)^o$	(7.4 ± 0.9) μm
η-correction	(45 ± 5) μm	$(0-1)^o$	(5.2 ± 1.0) μm
Weighted Mean	(85 ± 5) μm	$(5-7)^o$	(5.6 ± 0.9) μm

Future studies are underway to determine the angle and pitch dependent parameters which will be implemented in the LHCb VELO cluster position software tools.

[1]Corresponding author: arasp@nikhef.nl

Contents

1 Introduction

As part of the LHCb VELO detector commissioning, two consecutive test beam experiments were carried out to characterise the detector response. Particle tracks through six fully equipped silicon sensor modules were obtained by either beam-module interactions with a 400 GeV/c proton beam, or secondaries from beam-target interactions with a 180 GeV/c mixed hadron/muon beam. In this study, the main interest is the position reconstruction and the spatial resolution obtained from the track reconstruction. Various methods are available for determining the particle intersect position in a silicon strip detector. Studying the effects of inter-strip distance (pitch) and track inclination on the charge distribution among strips gives insight into the efficiency of cluster position reconstruction. A subset of the modules are used as a beam telescope to extrapolate tracks to a remaining module and make a comparison between the true and reconstructed intersect position.

In Section 2, the experimental setup during the November 2006 "Alignment Challenge and Detector Commissioning" (ACDC3) test beam and the general detector layout is described briefly. The various methods used for reconstructing the track position from the measured strip signal(s) are described in Section 3. This study focuses on 2-strip clusters from R-type sensors. Section 4 describes the charge distribution around the track intercept position. The spatial resolution obtained as a function of strip pitch and track angle for 2-strip clusters is presented in Section 5. Section 6 summarises the main conclusions.

2 Alignment Challenge & Detector Commissioning

Several ACDC phases in the LHCb VELO project were carried out towards the installation of the detector at the interaction point in the LHC. The first phase, ACDC1, exercised the read-out and analysis of data from multiple TELL1 boards with signal patterns. In ACDC2 and ACDC3, three and ten modules respectively were mounted in the North Hall experimental area. During the ACDC3 test beam, six of the ten double-sided silicon sensor modules could be read-out simultaneously with 12 TELL1 boards. The detector half was operated under vacuum (10^{-3} mbar) with the modules cooled down ($< 0\,^oC$) by a scaled down version of the final mixed-phase CO_2 cooling system [1, 2]. Figure 1 shows a schematic overview of the mounted modules. The coordinate system used was identical to that used by the LHCb detector.

Most of the tracks recorded through the detector originated either directly from the beam or are due to beam interactions with the vacuum vessel. This resulted in a big sample of tracks perpendicular to the module surface. Angled data ($1^o < \theta < 7^o$) were obtained from secondary particles from interactions with a lead target. A configuration in which the entire detector setup was rotated in the zy-plane was used to produce 8^o tracks through the modules.

Each module consists of two 300 μm thick n-on-n silicon sensors of which one is fitted with radial silicon strips to measure the ϕ angle (Φ-sensor) and the other is fitted with concentric strips to determine the radial position (R-sensor). Both geometries are shown in Figure 2. The inner(outer) radius amounts to 8 mm (42 mm). The pitch between strips increases linearly with radius from 40.0 μm to 101.6 μm for each of the four regions

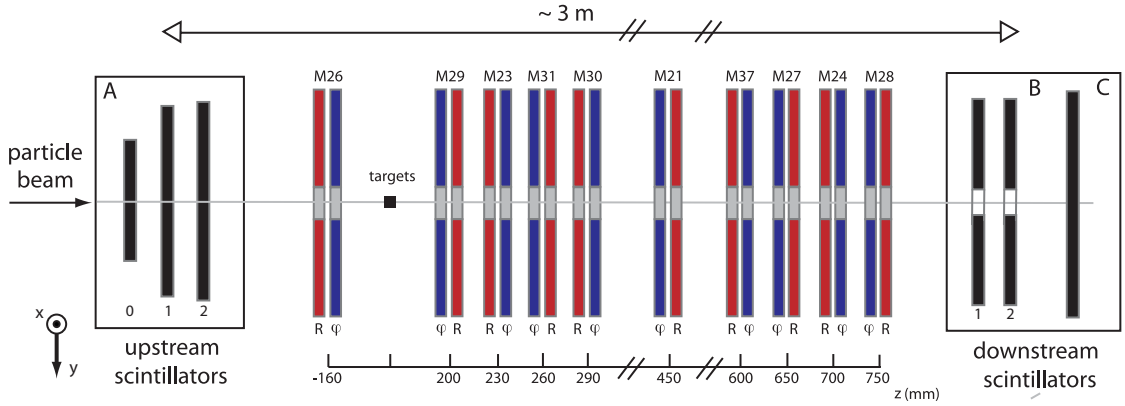

Figure 1: *Schematic top view of the ACDC3 detector setup. A total of ten modules (numbers correspond to the module numbering) were mounted in the detector half. Beam interactions with a target installed at x=y=z=0 were used to study high angled tracks.*

in R-type sensors. For ϕ-type sensors, the inner region has a pitch from 35.5 μm to 78.3 μm while for the outer region ranges from 39.3 μm to 96.6 μm . A change in stereo angle between the inner and outer region is implemented in order to reduce ambiguities in the pattern recognition. Furthermore, the detector modules are flipped from station to station ($R\phi, \phi R, R\phi$...). Details about the VELO detector can be found in [3, 4].

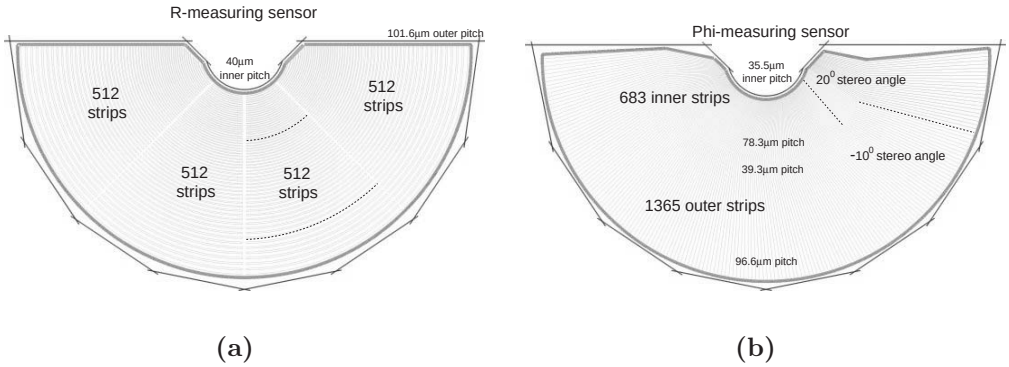

(a) **(b)**

Figure 2: *VELO R-type (a) and ϕ-type (b) sensor design. Each sensor has 2048 read-out strips covering the silicon surface. Notice the dog-leg shape in the Φ-sensor design due to the 20° and -10° stereo angles.*

A trigger logic based on three scintillators placed upstream and three scintillators placed downstream is used to trigger event read-out to the central data acquisition system (DAQ) [5]. The trigger decisions are sampled with the 25 ns clock cycle of the read-out supervisor (ODIN), using a 1.75 ns sampling window. After the trigger decision, the analog data is transmitted from the front-end Beetle chips to the TELL1 boards. Here, the analog data is digitised and further processed. More information on the Beetle, trigger scheme, TELL1 board and software can be found in [6, 7]. During the ACDC, the final LHCb processing hardware was used and strips with a signal exceeding 10 ADC counts were used to seed clusters. Neighbouring strips with a signal above 4 ADC counts were

also included in the cluster. The processing from raw data to clusters is called Zero Suppression (ZS).

During the data acquisition in the test beam, the module parameters (e.g. noise levels, temperatures) were continuously monitored. The data quality was monitored offline using the specially developed Vetra software package[2]. Both raw data (non-ZS) and ZS data could be analysed using this software.

In the pattern recognition and track fitting algorithms, the cluster positions are used to reconstruct tracks. Due to the differences in event characteristics between the ACDC and the LHCb experiment, a generic version pattern recognition has been implemented in the software (PatVeloGeneric, for more details see [8]). A non-iterative matrix inversion technique described in [9] is used to determine the alignment parameters for each setup. Data from dedicated alignment runs are used to produce alignment parameters for all degrees of freedom (translations and rotations). A track fit based on Kalman filtering is used to reconstruct the particle tracks through the modules. The reconstructed track along with the cluster information of all involved clusters is stored for further analysis.

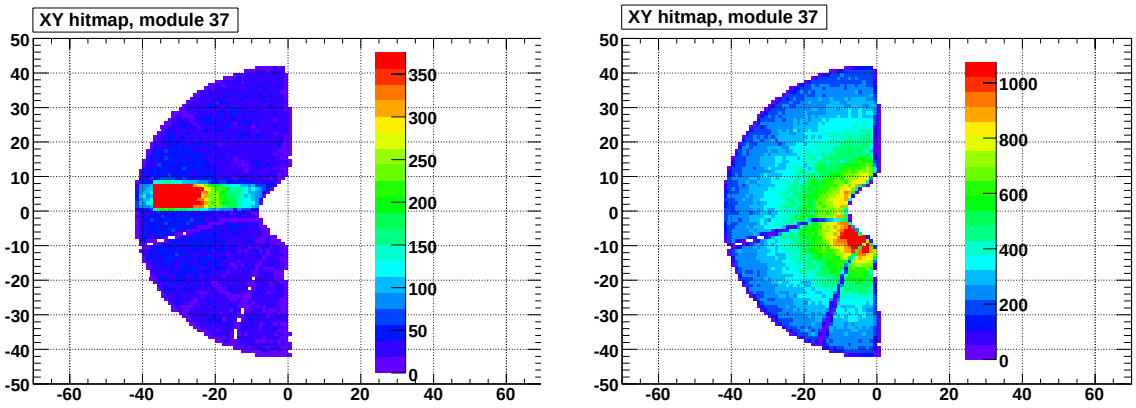

(a) Beam experiments **(b)** Target experiments

Figure 3: *Cluster position hitmaps from beam (a) and target (b) interactions in module M37. Notice the clear flux increase near the beam region during the target run.*

3 Reconstructing the track intercept position

With the track information available, a loop over all associated clusters is performed. For each cluster, the track cluster bank excluding the cluster in the sensor under investigation is used to refit the track. In this way, an unbiased track state is obtained which is extrapolated to the sensor under investigation. Important in this analysis is the *projected* angle, which is defined as the component of the track angle in the plane perpendicular to the local strip orientation. The intercept point between the sensor and the track is

[2]This software package is a smaller version of the official Brunel analysis software used in the LHCb experiment containing only the necessary VELO elements, in particular the facility to deal with non-ZS data.

assumed to be the true position of the cluster. For 2-strip clusters in R-sensors, on which this study focusses, x_0 is defined as the distance between the true position and the strip with the lowest number.

The analysis of non-ZS data shows strip noise ranging between 1.7 to 2.9 ADC counts after pedestal subtraction and common mode noise correction. The variation is mainly a result by different strip lenghts. The most probable value (MPV) of the charge deposition in a sensor is in the range of (49 ± 1) ADC counts. At an 8 degree angle, the increase in path length through a 300 μm sensor is approximately 1% and therefore the difference in amount of free charge carriers is minimal within the angle range. In this study, 2-strip clusters from R-sensors were used in the analysis due to the more complicated strip layout of the Φ-sensor. However, the Φ-sensors are expected to have identical characteristics in this respect.

The spatial resolution of the position reconstruction improves with the number of strips (n) in a cluster [10]. For 1-strip clusters, only binary accuracy is possible, while for multi-strip clusters the weighting of strip charges can be used to determine the intersect position between strips in the cluster. In the VELO clustering algorithm the maximum cluster size is limited to 4 strips. Three methods for reconstructing the intersect position are explained in the following sections.

3.1 Binary

In this method, only the strip with the highest S/N is considered and consequently determines the cluster position x_{rec}. The absolute error that follows is then half the strip pitch, $\Delta x_r ec = pitch/2$. The resolution of the 1-strip cluster position distribution is defined by the root-mean-square deviation,

$$\sqrt{<\Delta {x_{rec}}^2>} = \sqrt{\frac{1}{p}\int_{-p/2}^{p/2} x^2 \mathrm{d}x} = \frac{p}{\sqrt{12}}. \tag{1}$$

As can be seen, the resolution depends only on the local strip pitch. For the VELO R-sensors this ranges from 11.5 μm to 30.6 μm.

3.2 Weighted mean

During the charge drift time in the silicon, thermal diffusion will result in an increased charge spread at the sensor surface at which the strips are located. Furthermore, a small rearrangement of charge will also be present due to charge sharing between strips [11]. The position reconstruction is expected to improve when including these effects by a linear weighted mean approximation of strip charges [11, 12]. The position x of the cluster centre relative to the inner strip of the cluster is calculated using

$$x = \eta \cdot p \tag{2}$$

with

$$\eta = \frac{C_{\mathrm{outer}}}{C_{\mathrm{inner}} + C_{\mathrm{outer}}}, \tag{3}$$

where $C_{\mathrm{outer,inner}}$ stands for the signal at the strip associated to a cluster with the inner (outer) strip at the smaller (larger) radius. For example, when considering perpendicular

tracks ($\theta = 0^\circ$) crossing the silicon in between two strips an equal amount of charge is expected to be deposited on both strips and Eq. 3 results in η=0.5.

The true intersect position, x_0 is determined by using the remaining modules as a beam telescope. The associated error, Δx_0, can be significant due to the long extrapolation distances and (remaining) misalignments. The intersect positions are assumed to be spread Gaussianly around the true intersect position and the experimental resolution (σ_s) is determined from the width of this distribution. The η-range is binned with $\Delta\eta = \pm 0.02$ and the mean and mean-variance are used in the η-plots. The resulting curves are shown in Figure 4 for track angles increasing from 0° to 8° . On the vertical axis, the pitch normalised intersect position (x_0/p) is plotted.

In a few cases, a small offset in the η curve was measured which could result from remaining small sensor misalignments. The curves are therefore manually shifted to place the position η=0.5 at half the pitch ($x_0/p = 0.5$). Each of the curves is fitted with a third order polynomial,

$$\frac{x_\eta(\theta, p)}{p} = P_0 + P_1 \cdot \eta + P_2 \cdot \eta^2 + P_3 \cdot \eta^3, \tag{4}$$

in which the parameters $P_{0,1,2,3}$ are expected to depend on both θ and p. Due to noise influences on the strip charges, strip signals below 5 ADC counts are excluded from the analysis. This implies that in general the regions $\eta < 5/\text{MPV} \approx 0.1$ and $\eta > 0.9$ are excluded from the fit.

From the shapes of the various curves, it can be seen that the influence of the higher order terms of the fit reduces with increasing angle. In particular, above 4° a linear function can fit the data points within the measurement error. Only at large angles can the weighted mean method accurately estimate the true impact position. For smaller angles this is not the case. Here the η-function is curved at the lower and higher limit while it is only slightly inclined around half the pitch ($0.4 < x_0/p < 0.6$). In other words, only at half the pitch charge is measured at both strips while outside this region small angled tracks result mostly in 1-strip clusters. This explains the high fraction of 1-strip clusters observed in low angled tracks.

The diffusion width of the charge carrier cloud is independent of the pitch between the strips. As the distance between the strips is reduced, more charge is spread over multiple strips which would improve the weighted mean approximation. However, no change in the η-function was measured for perpendicular tracks. The diffusion width in a 300 μm silicon sensor is still small compared to the minimal R-sensor pitch (40 μm) and this can explain the non-linear η-function for (near) perpendicular tracks.

3.3 η-correction

A non-linear relationship is observed between the impact position and the charge ratio of signal strips, especially for low angled tracks (Fig. 4). In order to correct for this non-linear behaviour, the obtained fit parameters described in Eq. 4 are used in combination with the strip charges and local pitch. An iterative approach is thus required where the track angle is used in the first step to select the appropriate correction parameters $P_n(p, \theta)$. In the second iteration the parameters are used to recalculate the cluster position after which the track is refitted.

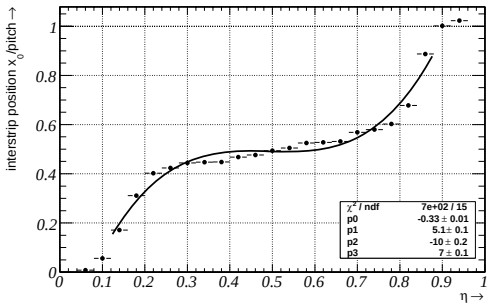

(a) 0°- perpendicular

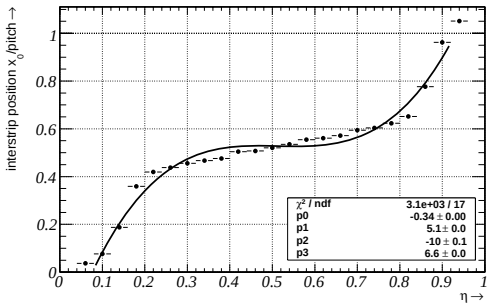

(b) 2°

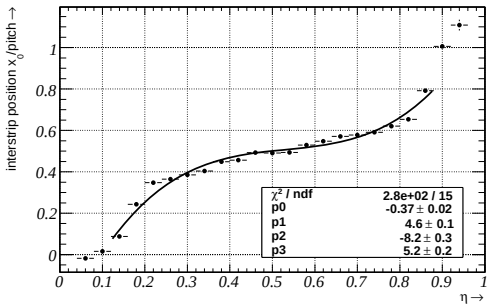

(c) 4°

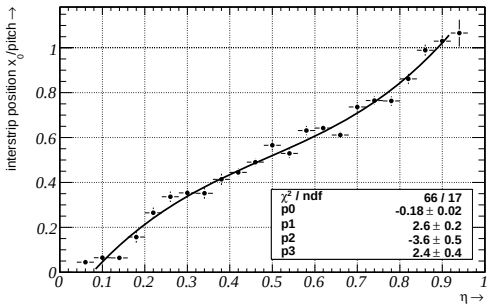

(d) 6°

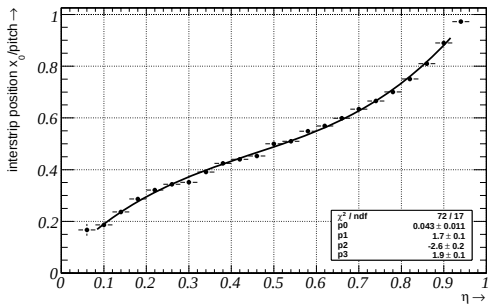

(e) 8°

Figure 4: *Normalised intersect point (x_0/p) versus strip charge ratio (η) for various track angles (0°,2°,4°,6°,8°). Data obtained during either beam or target interactions and summed for all R-sensors over the full pitch range. A third order polynomial function is fitted to the data points (line). Approximately 10^5 tracks were used to produce each plot.*

4 Charge Density Distribution

In the previous section the track angle influence on the shape of the $\eta(x)$-function was described. The strip charges are related to the Charge Density Distribution (CDD) at the sensor surface, which is the integrated charge profile over the sensor thickness. Studying the CDD allows for a qualitative and quantitative insight in the charge distribution due to diffusion and track inclination [11, 12, 13, 14, 15]. The procedure to determine the CDD at the strip surface from the test beam data is described in Appendix B. The resulting expression can be written as

$$C(s) = \frac{A}{\sqrt{4\pi L d^2}} \int_0^d \frac{1}{\sqrt{y}} \exp\left(\frac{-(s - s_0 - y tan(\theta))^2}{2Ly}\right) \mathrm{d}y, \tag{5}$$

where L is a function depending on the diffusion coefficient $D = kT\mu_i/q$ and the electric field, s the lateral distance from the intersect position ($x_{\text{true}} \pm s$) and θ, the projected angle of the particle track in the plane perpendicular to the local strip geometry. A large angle through the silicon will cause the profile to broaden and become asymmetric. A significant part of the total signal can therefore be collected on neighbouring strips.

Figure 5 shows the measured CDD curves for various angles (0°, 2°, 4°and 8°) from either beam or target interactions. Horizontally, the displacement around the track intersection point, s, is shown and vertically, the charge density scaled to the maximum value. To acquire enough statistics at various angles, track clusters with $\Delta\theta = \pm 1°$ were used in the analysis. The pitch range is binned with a width of $\Delta p = \pm 5\ \mu m$. All the distributions are fitted with the CDD function (Eq. 5) using the fitting parameters: *Constant* [A], *Theta* [tan(θ)], *Offset* [s_0] and *Sigma* [L]. Former studies of the CDD suggest the addition of an initial charge spread which would reduce the initial peak contribution [13, 14]. However this procedure was found to decrease the fit performance.

For perpendicular tracks through the sensor, the CDD is expected to display a profile that is mainly the result of charge carrier diffusion in the silicon (Fig. 5(a)). A symmetric profile around the intersect position is clearly visible and in agreement with the presented diffusion model. The average diffusion width over the sensor thickness is approximately 4.7 μm for a fully depleted sensor [11]. This number is expected to be roughly the same as the Full Width at Half Maximum (FWHM) of the CDD. This agreement is confirmed by the CDD in Figure 5(a) which shows a FWHM of 12 μm.

The largest charge density is measured at the position where the track passes closest to the strips. At this position, charge carriers are unable to diffuse due to the limited drift time to the surface. For perpendicular tracks, the track exit position is at the intersect position and therefore no offset is measured. The offset is related to θ by $\tan(\theta)d/2$. At the average pitch and track angle, the offset would be 5.2, 10.5 and 21.1 μm for 2°, 4°and 8° respectively. The fitted values are in the range of these values when considering the fit errors.

The charge liberated further away from the collecting electrode in the silicon has a longer drift time to the surface and hence the diffusion width increases. Charge is distributed over a larger surface area which causes the CDD to broaden and drop. At the track exit position, the slope of the charge density is steep as most of the liberated charge is in a small interval. A gradual transition of the charge density profile is seen with angle. Overall, this results in a asymmetric shape of the CDD and a broadening at larger angles.

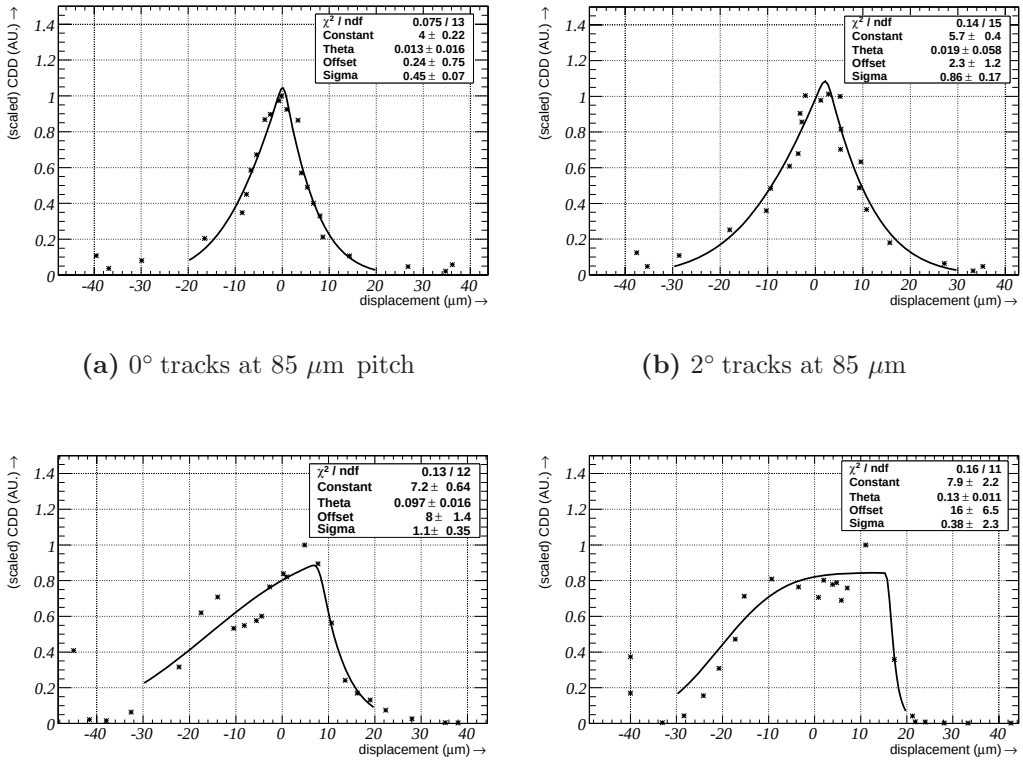

(a) 0° tracks at 85 μm pitch

(b) 2° tracks at 85 μm

(c) 4° tracks at 95 μm

(d) 8° tracks at 85 μm

Figure 5: *Charge Distribution Density (CDD) for various angles as a function of displacement around the track intersect point (s). For each plot, the average angle* ($\Delta\theta = \pm 1°$)*, source of the data file and the pitch region* ($\Delta p = \pm 5\,\mu$m) *are shown. Results for angled tracks from target interactions are obtained from sensors M24R, M27R and M30R. For the 8° distribution, modules M23R, M26R and M30R were used due to the different module configuration.*

For 8° tracks, the FWHM is measured to be approximately 35 μm at a pitch of 80 μm. A significant part of the total charge is thus spread over almost half the pitch. Compared to 0° tracks, the FWHM has increased by a factor 3.

An exact determination of the angle dependent parameter of the fit was found to be difficult due to the presence of large error bars on some of the data points. A clear increase is however visible and a reasonable agreement is seen for the high angled tracks, $\tan(4°) \approx 0.07$ and $\tan(8°) \approx 0.14$.

5 Spatial resolution

Experimentally, the sensor spatial resolution (σ_s) is obtained from the width of the residual distribution, where the residual is defined as the distance between the track intercept point and the cluster position. To reduce the influence of strip noise on the residual distribution only clusters are selected with both strip charges above 5 ADC counts. The presence of emitted δ-electrons in the silicon bulk can introduce a shift in the charge distribution.

High energy δ-electrons are therefore removed from the analysis by excluding clusters with total charges in excess of twice the MPV ($= 2 \cdot 50$ ADC counts).

The error on the true intersect position can be significant due to large extrapolation errors when the distance between the sensor and the beam telescope is large. This causes a further broadening of the residual distribution. Only the tracks with a high χ^2-probability are selected from the samples. Extrapolated tracks which do not intersect the sensor between the two cluster strips are also excluded. Figure 6 shows an example of the residual distribution determined from perpendicular tracks with either weighted mean (squares) or η-correction (circles) for perpendicular tracks. The weighted mean method results in a double peaked distribution where the distribution width is a combination of the intrinsic sensor resolution and the error associated with each track intercept point. To deconvolute the sensor resolution component an unbinned maximum likelihood fit was used. The fit assumes a Gaussian distribution for the residual distribution and returns the most likely sensor resolution given each measurement and its associated track error. The track error is taken from the covariance matrix of the track.

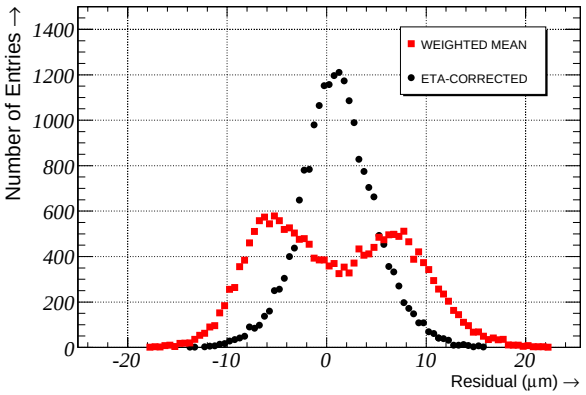

Figure 6: *Unbiased residual distribution using the weighted mean (squares) or $\eta(\theta, p)$-function (circles) in reconstructing the track cluster positions. Data points are for 2-strip clusters in M37R at 0 ° projected angle.*

Implementing the η-correction improves the reconstruction of the cluster position and results in a Gaussian distribution (Fig. 6). The width of the residual distribution is significantly reduced in this way.

5.1 Resolution versus strip pitch

In Figure 7, the sensor resolution is plotted as a function of pitch for 0° tracks for three position resolution methods. The data points for the binary resolution have been obtained with Eq. 1. The binary resolution increases linearly with pitch.

With the weighted mean method, the 2-cluster resolution is significantly improved. As the distance between the strips increases, the intrinsic sensor resolution deteriorates. For the widest pitch, $p = 100$ μm, σ_s is approximately twice as large as the value at the finest pitch. The best resolution for perpendicular tracks was obtained at $p = 45$ μm, $\sigma_s = (7.4 \pm 0.9)$ μm.

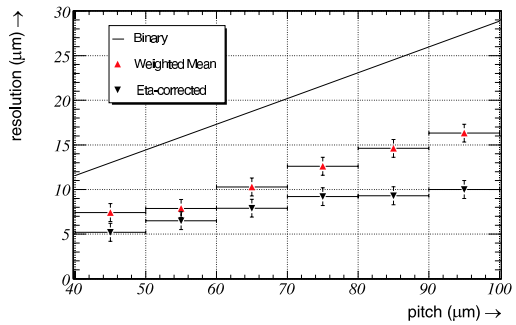

Figure 7: *Resolution versus pitch at 0° projected angle calculated with the weighted mean and η-correction methods. The solid line shows the binary resolution.*

Implementing the η-function parameters in the position reconstruction results in a further improvement of the resolution. This is most clearly obtained at the largest pitch region where the non-linear behaviour was most noticeable and thus the linear approximation is not sufficient. For perpendicular tracks the resolution in the finest pitch region ($p = 45 \pm 5$ μm) was measured to be 7.4 ± 1.0 μm. Applying the η-correction in the same pitch range improves the resolution, $\sigma_s = 5.2 \pm 1.0$ μm. The η-correction results in a resolution in the range of 5-10 μm over the full sensor pitch range.

5.2 Resolution versus track angle

Due to a change in the charge distribution with track angle, the sensor resolution is angle dependent. In Figure 8, the spatial resolution is plotted versus θ at a fixed pitch of $p = 85 \pm 5$ μm. For the weighted mean method, the resolution is expected to be of the following form [10],

$$\sigma_s(\theta) = \frac{A}{\theta^2 + B} + C\theta, \tag{6}$$

where A, B and C are constants that are determined in the fit. The shape of the curve corresponds well with simulations of angled tracks [10, 11]. A clear improvement in resolution is seen for tracks at angles above 4°. In this case, the η-function can be well approximated by the weighted mean of strip charges. This improvement is directly related to the broadening of charge density which results in a distribution of charges depending on the distance between liberated charge and the collection strip(s). More charge is thus able to reach neighbouring strips.

For the 0° and 2° cases, the η-function fit parameters were used in the analysis. It is seen that the resolution improves significantly. The non-linear behaviour at small angles can be well described by the correction. The best resolution measured with the weighted mean method at $p = 85$ μm and a track angle of 6° is $\sigma_s = 5.6 \pm 0.9$ μm. Overall, the estimate of the intrinsic sensor resolution is in the order of 8 ± 1 μm when using a generic reconstruction method. It must be noted that this resolution has been measured in the outer pitch region and further improvements are expected closer to the center of the sensor.

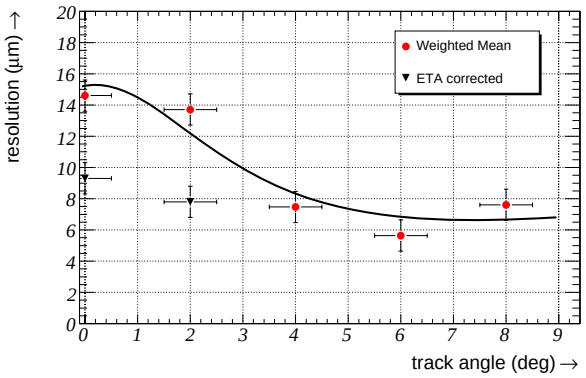

Figure 8: *Resolution versus angle at fixed pitch, $p = 85 \pm 5$ μm for weighted method (circles) and η-correction (triangles). Due to limited statistics, η-correction was only performed on 0° and 2° tracks.*

6 Conclusions

During the ACDC3 test beam, data from particles traversing the detector at projected angles ranging between 0° and 8° were collected and analysed. For perpendicular tracks, the Charge Density Distribution (CDD) is well described by lateral diffusion. The FWHM of the CDD was determined at approximately 12 μm. A clear influence of the track angle was seen in the collected charge profile at the strips. Liberated charge around the track path combined with charge diffusion in the silicon, resulted in a broadening of the CDD (FWHM of 35 μm at an 8° track angle).

The η-function was determined for various angles, relating the track intercept position to the 2-strip charge ratio. A non-linear relationship was seen at small track angles (<4°). In these cases, the width of the CDD is much smaller than the pitch between strips. For larger angles, the weighted mean of the cluster strip charges was determined to be a good estimate of the track intercept position.

The sensor resolution obtained in the VELO test beam experiments was determined from the unbiased residual distribution. The best resolution for perpendicular tracks was obtained at the finest pitch after applying the η-correction ($\sigma_s = 5.2 \pm 1.0$ μm). With the weighted mean method a resolution of (7.4 ± 0.9) μm was obtained. Increasing the pitch lowered the resolution (14.6 ± 0.1 μm at $p = 85$ μm for the weighted mean method). A study of the resolution versus angle showed a significant improvement with increasing angle. For 6° tracks at the above mentioned pitch of 85 μm a resolution of (5.6 ± 0.9) μm was obtained. For lower angles, the η-correction significantly improves the position reconstruction while for larger angles the weighted mean method is a good approximation.

One of the goals will be to incorporate the $\eta(\theta, p)$-curve parameters in the cluster position reconstruction. Preliminary investigations already showed a significant improvement in the resolution when applying the angle dependent η-function in the position reconstruction. Further investigations are being performed in this field.

Acknowledgments

The authors want to thank the SPS team for their excellent help in providing us with stable beam. The support of the LHCb on-line team in various stages of the project is greatly appreciated.

References

[1] B. Verlaat, *Controlling a secondary 2-phase* CO_2 *loop using a 2-phase accumulator*, International Congress of Refrigeration, ICR07-B2-1565, Beijing, 2007

[2] B. Munneke, B. Verlaat, A. Van Lysebetten, *Using the Blow System*. Online manual available at:
https://twiki.cern.ch/twiki/pub/LHCb/VeloBlowSystem/Blowsystem.doc

[3] LHCb Collaboration, *LHCb VELO Technical Design Report*, CERN/LHCC 2001-0011, TDR-5 (2001)

[4] LHCb Collaboration, *LHCb re-optimized detector design and performance : Technical Design Report*, TDR-9, CERN/LHCC 2003-030 (2003)

[5] M. Artuso, *ACDC3 Velo Test Beam*, Presentation available at:
http://indico.cern.ch/getFile.py/access?contribId=8&resId=1&materialId=slides&confId=8974

[6] S. Löchner et. al., *The Beetle Reference Manual*, CERN, LHCb-2005-105 (2005)

[7] G. Haefeli, *Contribution to the development of the acquisition electronics for the LHCb experiment*, PhD Thesis, EPFL (2004)

[8] T. Lastovicka, et al. *VELO Generic Pattern Recognition*, LHCb-2007-002 (2007), *to be published.*

[9] S. Viret, C. Parkes and D. Petrie, *LHCb VELO software alignment*, CERN, LHCb-2005-101 (2005)

[10] P. Bartalini, et al., *VELO Telescope Resolution and Efficiency Measurements*, CERN, LHCb-2000-099 (2000)

[11] P. Koppenburg, *A simulation of charge deposition and collection in silicon microstrip detectors*, IPHE 2001-001 (2001)

[12] G. Landi, *Properties of the center of gravity as an algorithm for position measurements*, Nucl. Instr. and Meth A, **485**, p698-719 (2002)

[13] M. van Beuzekom, *Identifying fast hadrons with silicon detectors*, PhD Thesis, University of Groningen (2006)

[14] E. Belau, et al., *Charge collection in silicon strip detectors*, Nucl. Instr. and Meth. A, **214**, p253-260 (1983)

[15] G. Landi, *Problems of position reconstruction in silicon microstrip detectors*, Nucl. Instr. and Meth A, **554**, p226-256 (2005)

[16] I. Johnson, et al., *A measurement of the Lorentz angle in silicon strip sensors at cryogenic temperature*, Nucl. Instr. and Meth A, **540**, p113-120 (2005)

A Derivation of the Charge Spread Function

A detailed description of the analysis of the charge spread caused by diffusion and track angle is presented here. For additional information see also [12, 14, 15, 16].
When a particle intersects the silicon sensor of thickness (d), charge is liberated along the particle track. These holes and electrons are separated by an applied electric field and depending on the type of silicon detector either the holes or the electrons drift to the read-out strips. The average drift velocity depends both on the charge mobility (μ_i with $i = e, h$ for electron/holes) and the local electric field ($E = V/d$). The charge carriers are accelerated in the direction of the E-field. It is assumed that to first order the electric field can be considered homogeneous over the detector thickness. The total time needed to fully collect the liberated charge can therefore be expressed as

$$t(y) = \frac{d}{V\mu_i} y, \tag{7}$$

where y is the distance between the charge carrier and the read-out strip ($0 < y < d$). Besides drifting in the electric field, charge carriers are also influenced by lateral diffusion in the silicon perpendicular to the applied field [11]. The scale of this diffusion (D) is related to the charge mobility and the operating temperature (T) of the material,

$$D_i = \frac{kT\mu_i}{q}. \tag{8}$$

Therefore the diffusion is different in magnitude for electrons or holes. The presence of diffusion causes the charge to spread as it crosses the sensor thickness. The Dirac-δ Charge Density Distribution (CDD) is subsequently broadened, where the diffusion causes a Gaussian spread around the position where the charges were liberated. The spatial charge distribution is generally given by

$$C(x, z, t(y)) = \frac{1}{2\pi Dtd} \exp\left(-\frac{(x - x_0)^2 + z^2}{2Dt}\right). \tag{9}$$

Resulting after integration in,

$$C(x, y) = \frac{1}{\sqrt{2\pi Ld}} \int_0^d \frac{1}{\sqrt{y}} \exp\left(-\frac{(x - x_0)^2}{2Ly}\right) \mathrm{d}y. \tag{10}$$

Here, several parameters have been collected in $L = Dd/V\mu_i$. Additionally, it is assumed that the primary charge distribution and the moment of ionisation is infinitesimally small.

Two cases can now be considered in the description. The case of straight tracks perpendicular to the xz-plane and tracks under an angle θ in the xy-plane. In the case of perpendicular tracks, the integral of Eq. 10 over the detector thickness results in a final distribution with a width proportional to the diffusion width [11]

$$\sigma_x(y) = \sqrt{2Dt(y)} = \sqrt{2L(d - y)}. \tag{11}$$

Figure 9 shows the CDD for 0° tracks after integrating over the detector thickness. The horizontal coordinate is the displacement around the track intercept point ($x_0 \pm s$) at $d/2$. In the angled case, the above description of the diffusion width is still valid. However, the point at which the charge is created is now shifted depending on the track inclination.

Due to this, integrating over the detector thickness in Eq. 10 becomes non-trivial. The distance x is transformed to $x = x \pm \tan(\theta)y$ [16][3]. The plus/minus-sign is related to the track geometry with respect to the detector layout. Rewriting the above equation results in,

$$C(s) = \frac{1}{\sqrt{2\pi L d}} \int_0^d \frac{1}{\sqrt{y}} \exp\left(\frac{-(s - s_0 \pm y tan(\theta))^2}{2Ly}\right) \mathrm{d}y. \tag{12}$$

In the case of a 0° angle, the original result is obtained. For higher angles, the track component results in a shifted charge distribution after travelling a distance Δy through the silicon. A numerical approach was followed to determine the charge distribution and this function was used for fitting the results with four free parameters: A, $\tan(\theta)$, s_0 and L. Here, A is an unknown amplitude related to the measurements and s_0, the offset of the function maximum. The black points in Figure 9 display the CDD for an 8° track angle.

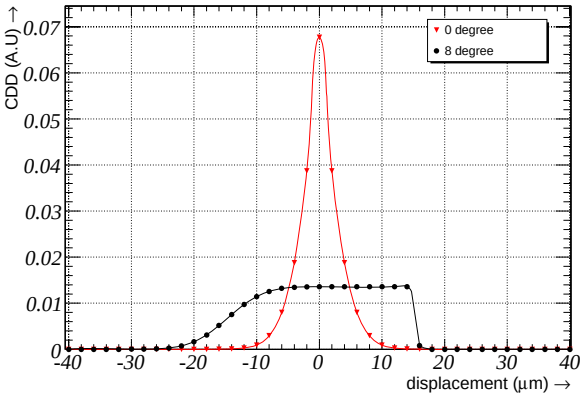

Figure 9: *Numerical calculations of the Charge Density Distribution function as a function of displacement around the track intercept point ($x_0 \pm s$) for 0° (triangles) and at 8° (circles) tracks.*

B Data analysis procedure

The fraction of the total charge, η, measured at the neighbouring strip in 2-strip clusters is given by

$$\eta = \frac{C_{\text{right}}}{C_{\text{left}} + C_{\text{right}}}. \tag{13}$$

From this expression, it is seen that the value of η is related to the charge density distribution around the track impact point. Specifically, the signal height at each of the strips neighbouring the track ($C_{\text{left,right}}$) can be expressed as an integral over the area they each cover of the Charge Density Distribution (see Eq. 12) [14]

$$C_{\text{left}} \propto \int_{-\infty}^{x_0} C(x)\mathrm{d}x, \qquad C_{\text{right}} \propto \int_{x_0}^{\infty} C(x)\mathrm{d}x. \tag{14}$$

[3]The description used in this paper is used in the case of track angles caused by a magnetic field component. Nevertheless, the procedure should be equivalent for the case of angled tracks.

Here, it is assumed that all the charge in a 2-strip cluster is collected at both strips and that the track intercept point at half the silicon thickness, x_0, is located in between the two strips. Furthermore, the amount of charge coupled to each of the strips by capacitive coupling is inversely proportional to the distance to the charge. After normalising the total pulse height to unity, the derivative of Eq. 13 to x can be expressed as

$$\frac{\mathrm{d}\eta}{\mathrm{d}x} = C(x). \tag{15}$$

Available from the measurements are the η-distribution, $\mathrm{N}(\eta)$, and the number of entries per x_0, $\mathrm{N}(x_0)$. Taking the derivative of the former to η, these can be related to Eq. 15 by

$$\frac{\mathrm{d}N}{\mathrm{d}\eta} = \frac{\mathrm{d}N}{\mathrm{d}x}\frac{\mathrm{d}x}{\mathrm{d}\eta} = \frac{\mathrm{d}N}{\mathrm{d}x}\frac{1}{C(x)}. \tag{16}$$

Concluding, the charge density around the impact position can be related to the change in $\Delta\mathrm{N}(x)$ per x interval, and inversely to $\Delta N(\eta)$. By repeating this procedure over the whole pitch range between two strips, the CDD as a function of s is obtained.